The Astrophysical Journal, 728:59 (13pp), 2011 February 10 doi:10.1088/0004-637X/728/1/59

POLYCYCLIC AROMATIC HYDROCARBON EMISSION WITHIN Lyα BLOBS

James W. Colbert[1], Claudia Scarlata[1], Harry Teplitz[1], Paul Francis[2], Povilas Palunas[3], Gerard M. Williger[4], and Bruce Woodgate[5]

[1] Spitzer Science Center, California Institute of Technology, Pasadena, CA 91125, USA
[2] Research School of Astronomy and Astrophysics, The Australian National University, Canberra, ACT 0200, Australia
[3] Las Campanas Observatory, La Serena, Chile
[4] Department of Physics & Astronomy, University of Louisville, Louisville, KY 40292, USA
[5] NASA Goddard Space Flight Center, Greenbelt, MD 20771, USA
Received 2010 August 2; accepted 2010 November 16; published 2011 January 20

ABSTRACT

We present *Spitzer* observations of Lyα blobs (LABs) at $z = 2.38$–3.09. The mid-infrared ratios (4.5 μm/8 μm and 8 μm/24 μm) indicate that ∼60% of LAB infrared counterparts are cool, consistent with their infrared output being dominated by star formation and not active galactic nuclei (AGNs). The rest have a substantial hot dust component that one would expect from an AGN or an extreme starburst. Comparing the mid-infrared to submillimeter fluxes (∼850 μm or rest-frame far-infrared) also indicates that a large percentage (∼2/3) of the LAB counterparts have total bolometric energy output dominated by star formation, although the number of sources with submillimeter detections or meaningful upper limits remains small (∼10). We obtained Infrared Spectrograph (IRS) spectra of six infrared-bright sources associated with LABs. Four of these sources have measurable polycyclic aromatic hydrocarbon (PAH) emission features, indicative of significant star formation, while the remaining two show a featureless continuum, indicative of infrared energy output completely dominated by an AGN. Two of the counterparts with PAHs are mixed sources, with PAH line-to-continuum ratios and PAH equivalent widths indicative of large energy contributions from both star formation and AGN. Most of the LAB infrared counterparts have large stellar masses, around $10^{11}\ M_{\odot}$. There is a weak trend of mass upper limit with the Lyα luminosity of the host blob, particularly after the most likely AGN contaminants are removed. The range in likely energy sources for the LABs found in this and previous studies suggests that there is no single source of power that is producing all the known LABs.

Key words: galaxies: evolution – galaxies: high-redshift – infrared: galaxies

1. INTRODUCTION

The Lyα blob (LAB) remains one of the great mysteries of the high-redshift universe. While these extended Lyα nebulae are similar in extent (5″–20″ or ∼50–150 kpc) and Lyα flux ($\sim 10^{43}$–10^{44} erg s^{-1}) to high-redshift radio galaxies, blobs are radio quiet and are therefore unlikely to arise from interaction with jets. They are found almost exclusively within high-redshift galaxy overdensities (Matsuda et al. 2009; Prescott et al. 2008; Palunas et al. 2004; Steidel et al. 2000) with none found so far at even moderate redshift ($z < 0.8$; Keel et al. 2009), suggesting strong evolution. After more than a decade of searching, there are still only a handful of the truly giant (>50 arcsec^2, $>5 \times 10^{43}$ erg s^{-1}) LABs known. However, deep searches (Matsuda et al. 2004; Saito et al. 2006) show that the blobs are part of a continuous size distribution of resolved Lyα emitters.

With most lying at the density peak of high-redshift structures (Matsuda et al. 2009, 2004; Palunas et al. 2004) and with number densities comparable to galaxy clusters in the nearby and high-z universe (10^{-5} to 10^{-6} Mpc^{-3}; Yang et al. 2009), it seems likely that the giant LABs are at the very least signposts for regions of massive galaxy assembly, if not the progenitors of the massive elliptical galaxies themselves. The limited *Hubble Space Telescope* imaging of these objects to date shows some evidence for interaction and merger of multiple compact objects (Chapman et al. 2004; Francis et al. 2001). Major mergers of high-mass galaxies, like those predicted to build giant ellipticals, must be occurring at higher redshift (i.e., Narayanan et al. 2010; Stewart et al. 2009). The LAB may represent an opportunity for the study of the merger formation of the most massive galaxies.

One of the biggest unknowns of the blobs is the source of their energy. Matsuda et al. (2004) found that for at least a third of LABs, including all the biggest and brightest of them, the galaxies within the blob do not emit enough rest-wavelength UV light to excite such a vast quantity of hydrogen gas. The exciting ultraviolet illumination could be escaping along different lines of sight from an obscured active galactic nucleus (AGN; Basu-Zych & Scharf 2004). Many LABs contain luminous X-ray counterparts (Geach et al. 2009; Yang et al. 2009), while others show powerful AGN emission lines (Scarlata et al. 2009; Dey et al. 2005; Pascarelle et al. 1996). Alternatively, outflows could be driving great plumes of gas into the surrounding ambient medium and producing shocks. While AGNs are known to drive some outflows, supernova-driven superwinds are also a viable model (Taniguchi & Shioya 2000; Ohyama & Taniguchi 2004). Such outflows would likely take the form of immense bubbles or shells expanding outward from the galaxy, some evidence of which has been claimed in the brightest LABs (Mori & Umemura 2007).

Integral field spectroscopy of the LABs shows the large Lyα velocity widths and structure consistent with superwind outflows (Bower et al. 2004; Wilman et al. 2005; Weijmans et al. 2010), although the systems are complicated enough that other velocity models, like rotation, cannot be completely ruled out. Cooling flows have also been suggested as a possible source of the extended Lyα emission (Haiman et al. 2000; Francis et al. 2001; Dijkstra et al. 2006). The primary evidence to support the cooling model is LABs with no apparent internal power source, even out to the mid-infrared (Nilsson et al. 2006; Smith et al. 2008), and sources with He II emission with weak to no measurable C IV emission (Prescott et al. 2009; Scarlata et al.

2009), indicative of the lower temperature gas emission that one would expect from a cooling flow (Bertone & Schaye 2010).

Mid-infrared and submillimeter imaging show that it is very common that the extended nebulae of LABs contain sources of extreme infrared luminosity. Powerful *Spitzer* 24 μm sources have been found within roughly 10 LABs, and almost all the most luminous ones, (Webb et al. 2009; Geach et al. 2007; Colbert et al. 2006b; Dey et al. 2005), with fluxes of 0.05–0.86 mJy. Submillimeter flux has been measured for a similar number (Chapman et al. 2004; Smail et al. 2003; Geach et al. 2005; Beelen et al. 2008). Mid-infrared colors suggest significant quantities of hot dust for these infrared-bright sources (Webb et al. 2009), although whether from AGN or extreme star formation remains unclear.

In this paper, we discuss mid-infrared and submillimeter observations of mid-infrared sources identified within LABs from four different fields, with $z = 2.38$–3.09. We examine both their *Spitzer* mid-infrared flux ratios and mid-infrared to submillimeter flux ratios and compare them to models in order to identify their likely power source, AGN or star formation. We then look at *Spitzer* Infrared Spectrograph (IRS) spectra of six sources for an even more definitive AGN/star formation separation. Finally, we look at the possible masses of these infrared sources from within the LABs. We assume an $\Omega_M = 0.3$, $\Omega_\Lambda = 0.7$ universe with $H_0 = 70$ km s^{-1} Mpc^{-1}.

2. DATA ACQUISITION AND REDUCTION

2.1. LAB Nomenclature

Because of their rarity, most LABs are discovered in small numbers, often one or two at a time. This has led to a naming system where the LABs in question are often just referred to as Blob 1 or Blob 2, if they are given any specific name at all. That creates a problem for a work such as this one, where multiple LABs are being discussed from multiple fields, all known as Blob 1 or LAB1 or B1 or something similar. Since LABs are large, they occasionally have multiple counterparts associated with them, which can make it even more difficult to identify the correct object under discussion.

To address this issue, we will use the following naming system in this paper. All LABs will be referred to as

LAB[number][letter]_J[coordinate of associated field center]

The [number] used is that which has been associated with the LAB in previous publications, if there has been any. If no previous number has been assigned, we will begin the labeling at LAB1 and count upward from there. In many cases, the original numbering included all the detected Lyα emitting sources in the field, so just because there is a LAB6 does not indicate that there must be a LAB5. While these "missing" numbers might create some mild confusion, we found this system to be superior to the certain confusion that would result from changing the numbers that have already been used to identify these sources from one paper to the next.

The [letter] refers to the counterpart of the LAB being discussed. Most blob counterparts have only one associated counterpart and will therefore be given no letter identifier, so the existence of a letter implies that at some point in the literature, multiple components have been assigned to the LAB. Discussions of the LABs themselves will never be given a letter.

The [coordinate of the associated field center] is an eight-digit code giving the right ascension and declination (J2000) of the field with which the LAB is associated. Most of these fields have been observed multiple times with slightly different centers, but for this paper we have chosen J2217+0017, J1714+5014, J1434+3317, and J2143−4423 to represent the SSA22, 53w002, NDWFS, and J2143−4423 fields in this study (see below). We found this method of only providing a field coordinate superior to a full 12–14-digit coordinate designation as it makes the discussion of object names significantly less cumbersome and keeps a clear connection with the field and/or structure they have been found within.

Table 1 provides the list of all the LAB infrared counterparts included in this paper, providing both the new name as well as any previous names by which the LABs have been known.

2.2. IRAC and MIPS Data

The LABs presented in this paper are spread across four different fields: J2143−4423, SSA22, 53w002, and the NOAO Deep Wide-Field Survey (NDWFS). We assembled all available *Spitzer* mid-infrared imaging data, which include both IRAC and MIPS imaging.

The data for the J2143−4423 field (LAB1_J2143−4423, LAB6_J2143−4423, LAB7_J2143−4423) come from GO-3699 (PI: Colbert) and were done in a 3 × 5 raster map covering 15′ × 25′, centered at $\alpha = 21^h42^m35^s$, $\delta = -44°27'$ (J2000.0). The total integration times per pixel were 1800 s for IRAC channels 1–4 and 1818 s for MIPS 24 μm. This reached 3σ depths of 1, 7, and 40 μJy for 4.5, 8, and 24 μm, respectively.

For the SSA22 field (see Steidel et al. 2000; Matsuda et al. 2004), we examine the 16 LABs with both an isophotal area greater than 20 arcsec^2 and submillimeter data coverage, excluding only LAB4_J2217+0017 which lies too close to a bright object for an uncontaminated analysis. We assembled the *Spitzer* imaging from multiple programs taken at different epochs, centered roughly at $\alpha = 22^h17^m40^s$, $\delta = +00°17'$ (J2000.0). The IRAC and MIPS data come from four programs: GO 30600 (PI: Colbert), GO 3473 (PI: Blain), and GTO 64 & GTO 30328 (both PI: Fazio). The IRAC data were previously presented in Webb et al. (2009), but we re-extracted the photometry to ensure uniformity among our several fields and also extracted to slightly deeper (3σ) depths. The MIPS data presented here include new data (GO 30600, see below) not presented in Webb et al. (2009), covering more sources and greatly increasing the 24 μm depth.

The SSA22 IRAC data from GTO 64 were a deep pair of single pointings covering most of the known SSA22 blobs, GTO 30328 was a 3 × 4 raster map, while GO 3473 was a smaller 2 × 3 raster map that lies to the east of the majority of the known LAB positions. Altogether the combined IRAC image maps out a region roughly 20 × 26 arcmin, ranging in depth from 1500 to 15,000 s. Most of the LABs lie at depths of 4000 s or greater, roughly corresponding to 3σ depths of 0.5 and 5 μJy at 4.5 and 8 μm, respectively. Only one of the submillimeter detected blobs (LAB10_J2217+0017) completely falls off the area covered by IRAC.

The SSA22 MIPS data come from GTO 64, a single pointing (1120 s), GTO 30328, a 3 × 3 map built from a set of cluster offsets (1200 s pixel^{-1}), and GO 3473, a set of pointings targeting known submillimeter galaxies (SMGs; 1200 s). GO 30600 consisted of two parts. The first was a set of three pointings targeting the submillimeter detected blobs on the outskirts of the previously taken 24 μm data (2700 s each). The second part was an extremely deep pointing on the central portion of the field (10,800 s) where the biggest LABs (LAB1_J2217+0017 and LAB2_J2217+0017; Steidel et al. 2000) are located. Assembled altogether the MIPS data cover an area roughly

Table 1
LAB Infrared Counterparts

Name[a]	4.5 μm Flux (μJy)	8 μm Flux[b] (μJy)	24 μm Flux (μJy)	850 μm Flux (mJy)	Lyα Lum (10^{43} erg s^{-1})	Mass Up. Limit (10^{11} $M_{\odot}$)	Previous Names
LAB1a_J2217+0017	8.6 ± 0.3	14.6 ± 1.2	25 ± 5	16.8 ± 2.9	11	2.0	Blob 1, LAB01-a
LAB1b_J2217+0017	10.7 ± 0.3	15.5 ± 1.2	47 ± 5	16.8 ± 2.9	11	2.4	Blob 1, LAB01-b
LAB2b_J2217+0017[c]	7.5 ± 0.2	10.1 ± 1.3	<10	3.3 ± 1.2	8.5	1.7	Blob 2, LAB02-b
LAB3_J2217+0017	11.1 ± 0.4	21.5 ± 1.6	38 ± 10	<3	5.8	2.5	LAB03
LAB5_J2217+0017	9.5 ± 0.3	14.8 ± 1.9	47 ± 6	5.2 ± 1.4	1.7	2.2	LAB05
LAB6_J2217+0017	4.3 ± 0.4	<9.4	n/a	<3.6	1.6	0.99	LAB06
LAB7_J2217+0017	2.5 ± 0.2	<4.6	<24	<3.2	1.5	0.57	LAB07
LAB8_J2217+0017	0.9 ± 0.1	<2.6	<10	<10.6	1.7	0.18	LAB08
LAB9_J2217+0017	3.6 ± 0.2	3.4 ± 1.4	53 ± 13	<10.6	1.3	0.87	LAB09
LAB10_J2217+0017	n/a[d]	n/a[d]	207 ± 12	6.1 ± 1.4	2.2	n/a	LAB10
LAB11_J2217+0017	2.3 ± 0.1	6.0 ± 1.1	<16	<10.6	0.91	0.53	LAB11
LAB12_J2217+0017	8.2 ± 0.3	10.1 ± 1.6	58 ± 5	3.2 ± 1.6	0.86	1.9	LAB12
LAB14_J2217+0017	10.3 ± 0.3	17.5 ± 1.4	63 ± 5	4.9 ± 1.3	1.2	2.4	LAB14
LAB16_J2217+0017	7.3 ± 0.2	14.0 ± 1.4	80 ± 5	<10.6	0.99	1.7	LAB16
LAB18a_J2217+0017[e]	8.4 ± 0.3	21.2 ± 2.4	159 ± 10	11.0 ± 1.5	0.64	2.9	LAB18-a
LAB19_J2217+0017	1.8 ± 0.1	<2.4	<24	<10.6	1.3	0.41	LAB19
LAB20_J2217+0017	0.5 ± 0.1	<2.4	<10	<3.0	0.64	0.096	LAB20
LAB1_J2143−4423	24.7 ± 3.3	24.7 ± 5.0	236 ± 37	<1.7	7.9	3.6	B1
LAB6a_J2143−4423	58.0 ± 5.0	189 ± 12	542 ± 34	<2.0	6.2	7.5	B6-Ly1
LAB6b_J2143−4423	34.7 ± 3.9	50.7 ± 6.3	640 ± 36	4.9 ± 2.0	6.2	4.9	B6-Ly2
LAB7_J2143−4423	21.4 ± 3.1	23.4 ± 5.0	292 ± 30	8.4 ± 1.0	3.1	3.1	B7
LAB18_J1714+5015	19.3 ± 0.6	73.5 ± 2.6	700 ± 28	5.6 ± 0.9	5.1	2.9	Obj. 18
LAB19_J1714+5015	44.1 ± 1.3	56.4 ± 2.2	200 ± 9	<0.9	2.1	6.8	Obj. 19
LAB1_J1434+3317	26.3 ± 3.1	77.0 ± 14.9	860 ± 50	n/a	17	4.8	SST24 J1434110 +331733

Notes.
[a] Primary LAB reference for each field—J2217+0017 (SSA22): Matsuda et al. (2004); J2143−4423: Palunas et al. (2004); J1714+5015 (53w002): Keel et al. (1999); and J1434+3317 (NDWFS): Dey et al. (2005).
[b] All limits listed are 2σ.
[c] We found only one source with 8 μm flux bright enough to be a likely infrared counterpart. It had been previously labeled as counterpart "b" (Geach et al. 2007). We keep the "b" label for this source, but there is no counterpart "a" used in our analysis.
[d] The counterpart to LAB10 falls just off the IRAC channels 2 and 4 fields, but not IRAC channel 1 (16.0 ± 0.5 μJy) or channel 3 (28.9 ± 2.0 μJy).
[e] We do not find the object "b" (Webb et al. 2009) to be a likely counterpart—it is faint at 24 μm and offset by 7″—so it is not included in our analysis.

15 × 26 arcmin, with the regions covering the LAB locations ranging from 1200 to 13,000 s, with all submillimeter detected LABs observed for at least 3300 s, which provides a 3σ depth of ∼30 μJy.

The 53w002 field, centered at $\alpha = 17^{h}14^{m}20^{s}$, $\delta = +50^{\circ}15'$ (J2000.0), contains two LABs (Keel et al. 1999). The IRAC data come from GTO 211 (PI: Fazio) and were obtained in a single pointing of 3300 s in all four IRAC bands. The MIPS data are a combination of GO 3329 (PI: Stern), a single 500 s pointing, and GO 20253 (PI: Im), a much deeper exposure of 18720 s. The 3σ depths obtained are 0.6, 5, and 12 μJy for 4.5, 8, and 24 μm, respectively, not accounting for the effect of confusion noise which becomes significant in such a deep 24 μm pointing. Both blobs in the field have mid-infrared counterparts that are bright enough that confusion is not an issue.

The NDWFS contains one reported bright blob (Dey et al. 2005), located at $\alpha = 14^{h}34^{m}11\overset{s}{.}0$, $\delta = +33^{\circ}17'31''$ (J2000.0). We do not attempt to re-reduce or extract new photometry for this source and use the IRAC and MIPS fluxes already reported in Dey et al. (2005).

Both the IRAC and MIPS data were combined using the MOPEX package available from the *Spitzer* Science Center (SSC). For the IRAC data, we started with the artifact-mitigated (.cbcd) files where available (GTO 30328). For the programs that had not yet been reprocessed above pipeline S16 (the first .cbcd files begin at S17), we used the basic bcd and applied the IRAC Artifact Mitigation code (available from the SSC) ourselves. For our extragalactic fields, which contain very few bright stars or extended sources, we saw no significant difference between the two methods. We then removed a residual offset from each frame by subtracting the median of each frame itself (i.e., removing a constant sky), medianing all the subtracted frames, and then subtracting that resulting offset frame from all the original frames. This prevents a gradient from appearing in the final images. This is the data product we place into MOPEX to produce the final, combined image.

For the MIPS data, a median flat was created from all available data taken near in time, normalized, and divided into each image. After the Overlap Correction module was executed by MOPEX, we found that we still had some trouble getting all the various sky levels to match up, so an additional sky constant was also subtracted before final combination of all the MIPS frames.

2.3. Optical and Near-infrared Data

The optical and NIR data for the J2143−4423 field (U, B, G, R, J, and H) were acquired at the Cerro Tololo Inter-American Observatory (CTIO) 4 m telescope, using the Mosaic II imager, and the near Infrared Side Port Imager camera (ISPI). The seeing

Table 2
IRS LAB Targets

Name	R.A.	Decl.	Redshift	24 μm Flux (μJy)	Int. Time (minute)
LAB1_J2143−4423	21h42m27.63s	−44d20m30.3s	2.38	240	528
LAB6a_J2143−4423	21h42m42.80s	−44d30m18.0s	2.38	540	120
LAB6b_J2143−4423	21h42m42.65s	−44d30m09.2s	2.38	630	120
LAB7_J2143−4423	21h42m34.99s	−44d27m08.5s	2.38	290	264
LAB18_J1714+5015	17h14m11.98s	+50d16m01.5s	2.39	590	84
LAB1_J1434+3317	14h34m10.98s	+33d17m30.9s	2.66	860	52

ranged from 0.″9 to 1.″4, reaching depths of ∼26 for U and B, ∼24 in R, and ∼23 in J and H. For further details, see Scarlata et al. (2009). All magnitudes are AB magnitudes here and throughout the paper.

2.4. IRS Spectra

As part of the *Spitzer* GO 30600, we targeted all known bright (>200 μJy) 24 μm sources associated with LABs, including those within the J2143−4423 110 Mpc filament structure at $z = 2.38$ (Palunas et al. 2004; Colbert et al. 2006b) and one within the possible protogalaxy structure around radio galaxy 53w002 at $z = 2.39$ (Pascarelle et al. 1996). Altogether we targeted five mid-infrared sources associated with four LABs. LAB6_J2143−4423 contains two powerful MIPS 24 μm sources (Colbert et al. 2006b), both of which have been confirmed to be at the redshift of the blob (Scarlata et al. 2009). At the time of observation, there was one more known mid-infrared-bright (0.86 mJy at 24 μm) LAB1_J1434+3317 discovered in the NDWFS by Dey et al. (2005) for which IRS spectra had already been taken. We include its IRS data as part of our analysis. The complete list with coordinates is presented in Table 2.

There are no >200 μJy 24 μm-emitting LABs in the most well-studied LAB field of all, the $z = 3.09$ SSA22 field (Steidel et al. 2000), despite many of them having significant submillimeter detections. This is likely the result of the strong 7.7 μm feature having shifted out of the MIPS 24 μm filter. For these sources, we only examine their mid-IR to submillimeter ratios.

The mid-infrared spectra were all taken with the *Spitzer* IRS using the first order of the Long-Low module (LL1), which is sensitive from 19.5 to 38.0 μm. The LL1 module has a spatial resolution of 5.1 arcsec pixel^{-1} and a wavelength resolution of $R = 58$–116, with the $\Delta\lambda$ an approximately constant 0.17 μm pixel^{-1}. The aperture of the LL1 long slit is 10.7 × 168 arcsec.

The IRS data were acquired from the *Spitzer* cycle 3 GO 30600 program, mostly taken on 2007 June 13–21, although one spectrum (LAB18_J1714+5015) was taken on 2006 September 16. These spectra were acquired using the IRS Spectral Mapping Astronomical Observation Template (AOT), placing the source at six separate positions along the length of the slit, each separated by 20″. A high accuracy peak-up observation on a nearby Two Micron All Sky Survey star was done for each observation. We used the 120 s ramp exposure throughout, producing total exposure times per source of 84–528 minutes.

We began our data reduction with the Basic Calibrated Data (BCDs) produced by the *Spitzer* pipeline S16.1. A significant latent charge builds up on the detector over long observations that varies depending on wavelength. To correct this, we measure a median background value for each wavelength row and then fit a slope to the change in background with time. Using the slope at each wavelength, we derive the corresponding latent buildup for each frame and subtracted it.

We then averaged together all the exposures taken at the same position within each Astronomical Observation Request (AOR), producing six two-dimensional spectra per AOR. We also produced a separate sky frame for each position using all the images taken at the other five positions medianed together. We subtracted each sky frame from its corresponding image and then ran the program IRSCLEAN, provided by the SSC, in order to remove all remaining rogue pixels or cosmic ray strikes. We then extracted the one-dimensional spectra for all six positions using the optimal extraction option within the SSC tool SPICE (v.2.1.2). We used a smaller than standard aperture (5 pixels at 27 μm, width scaling with wavelength) in order to avoid flux from two nearby bright sources and to reduce the inclusion of noise from blank sky. This non-standard aperture alters the SPICE generated calibration, but we use the known 24 μm fluxes for final calibration so this was not an issue.

The initial sky subtraction does not always produce a perfect zero background and cannot account for contamination from brighter, nearby sources. To address this, we extracted one-dimensional sky spectra using the same method and aperture as that for the sources, only offset by 30 arcsec. Two sky spectra, one from each side, are extracted, except for the spectra closest to the edge of the slit, where only one is extracted. We median all the sky spectra together and apply a 1.7 μm wide boxcar smoothing, before subtracting this one-dimensional sky from the extracted source spectra. This secondary sky subtraction adds ∼2%–5% to the noise of the extracted source spectra, but can make significant corrections to the spectral shape, particularly in the two cases (LAB1_J2143−4423 and LAB7_J2143−4423) with bright nearby sources.

Finally, we average the spectra from all the positions into a final spectrum using a 2σ clipping. In the case of LAB1_J2143−4423, the data were taken in two AORs with slightly different roll angles. This minor difference in position angles produced a large difference in the contamination from a nearby quasar, producing significantly more noise (60% higher). Therefore, we applied a variance weighting to the combination the LAB1_J2143−4423 spectra. In all the other cases, the noise was constant across spectra and no weighting was required.

As part of our analysis, we also include one IRS spectrum (LAB1_J1434+3317) taken as part of the GTO 15 program in 2005 February and June. This spectrum was taken using the IRS Staring AOT, which takes exposures at two separate positions along the slit length, separated by ∼55 arcsec. Because of the smaller number of positions, instead of subtracting a two-dimensional medianed sky from each position we simply subtracted one nod from the other. We also note that the BCDs were produced by the S15.3 pipeline. Otherwise the data

reduction is identical to those spectra taken in IRS Spectral Mapping mode.

3. PHOTOMETRY

The LABs are large and commonly cover multiple IRAC sources, so we used the positions of the brightest IRAC 8 μm sources as the likely source of any 24 μm or 850 μm emission. This approach produced a good match between the centers of the associated 8 and 24 μm sources in all cases where both are strongly detected. For sources with no 8 μm detections within the blob (5 sources from SSA22), the position of the 3.6 μm source within the LAB is used. None of the sources without 8 μm detections had 24 μm or 850 μm detections, meaning that they are not included in most of the following analysis of flux density ratios.

Two sources had multiple strong 8 μm sources, each with measurable 24 μm fluxes, within the LAB: the LAB6_J2143−4423 (Colbert et al. 2006b; Scarlata et al. 2009) and LAB1_J2217+0017 (Geach et al. 2007; Webb et al. 2009). For the case of LAB6_J2143−4423, an examination of the full spectral energy distribution (SED) and IRS spectra (see Scarlata et al. 2009, and below) reveals that the counterpart LAB6a_J2143−4423 is powered by an AGN while LAB6b_J2143−4423 is powered by star formation, making it almost a certainty that the submillimeter flux identified at that position is coming from LAB6b_J2143−4423 and all further analysis assumes the same as well. The two sources in LAB1_J2217+0017, on the other hand, have very similar mid-IR colors, so it is not possible to discriminate from which 8 μm source the submillimeter might have originated. Using both OVRO and VLA 21 cm observations, Chapman et al. (2004) found emission near the most northern of the two 8 μm objects (LAB1a_J2217+0017; Geach et al. 2007). However, there is evidence that the 850 μm flux for this source is likely distributed across multiple sources (Matsuda et al. 2007), indicating that the second 8 μm source (LAB1b_J2217+0017) may also be a significant contributor to the total submillimeter flux. For our analysis of 24 μm/850 μm, we therefore combined the two sources together (see more below).

MIPS 24 μm photometry was derived from PRF-fitting using APEX, part of the *Spitzer* MOPEX software tool (Makovoz & Marleau 2005). In the cases of 24 μm non-detections, we extracted limits from the data using the known 8 μm positions. The rest of the photometry was done using apertures. For the U, B, R, J, and H bands, we derived the flux densities using apertures of radius ∼1.5 × FWHM (1.″72, 2.″10, 1.″95, 1.″35, and 1.″35). For the IRAC channels 3 and 4, we used a 3.″6 aperture, but for channels 1 and 2 we used a 2.″4 aperture to avoid crowding issues. All the above apertures only required moderate aperture corrections of 10%–22%.

Substantial submillimeter imaging has been published on many of the major fields known to contain LABs, including the $z = 3.09$ SSA22 field (Geach et al. 2005; Chapman et al. 2004), the $z = 2.38$ J2142−4423 cluster (Beelen et al. 2008), and the $z = 2.39$ 53w002 field (Smail et al. 2003).

The SSA22 field was imaged at 850 μm using the Submillimetre Common User Bolometer Array (SCUBA) on the James Clerk Maxwell Telescope reaching 1σ noise limits of 1.5 mJy using the pointed photometry mode and 5.3 mJy from a more shallow scan-map. Five blobs were detected with fluxes ranging from 4.9 to 16.8 mJy (Geach et al. 2005). All but the brightest one were found in the deeper pointed observations. There are also Submillimeter Array (SMA; Matsuda et al. 2007) and Atacama Submillimeter Telescope Experiment (ASTE; Kohno et al. 2008) observations of the brightest blob (LAB1_2217+0017) in the field.

The J2143−4423 cluster was imaged at 870 μm (345 GHz) using the LABoCA (Siringo et al. 2007, 2008) instrument installed on the Atacama Pathfinder Experiment (APEX; Güsten et al. 2006) reaching a 1σ point source sensitivity of 1.4–7 mJy, depending on distance from center of the field. LAB7_J2143−4423 is robustly detected (8.4 ± 1.0 mJy), while LAB6_J2143−4423 is only marginally detected (4.9 ± 2.0 mJy).

The SCUBA 850 μm observations of the 53w002 field reach 1–1.5 mJy noise levels and detect one of the two known blobs there (LAB18_J1714+5015; 5.6 ± 0.9 mJy).

For ease of discussion, the rest of the paper will use 850 μm to describe either the 850 μm SCUBA data or the 870 μm LABoCA data. It is assumed that at the level of accuracy of the reported submillimeter fluxes there are no measurable differences between the two submillimeter bands.

We present the flux densities of all the LAB counterparts presented in this paper in Table 1.

4. RESULTS

4.1. Spitzer Flux Density Ratios

The mid-infrared properties of warm ULIRGs, those dominated by AGN radiation, are significantly different from those of cool ULIRGs powered by star formation. The SEDs of warm ULIRGs rise rapidly and steadily through the mid-infrared, roughly obeying a power law, while the cool ULIRG SEDs do not rise steeply until far into the mid-infrared (>10 μm). The other significant difference is the presence of strong polycyclic aromatic hydrocarbon (PAH) features in cool ULIRGs, which can be compared to the continuum to determine the fraction of infrared luminosity generated by star formation (Lutz et al. 1998; Rigopoulou et al. 1999).

Because of these mid-infrared color differences, plots of *Spitzer* mid-infrared IRAC colors can be powerful tools for identifying AGN and separating them from starbursts at low redshifts (Stern et al. 2007, 2005; Lacy et al. 2004). By including MIPS 24 μm, one can then continue this analysis to much higher redshift (i.e., Webb et al. 2009; Pope et al. 2008). We plot all the mid-infrared sources associated with LABs that have 8 μm detections in Figure 1, which is a comparison of the 24/8 μm flux density ratio to the 8 μm/4.5 μm flux density ratio.

Both Webb et al. (2009) and Pope et al. (2008) created just such a mid-infrared color–color plot for their respective samples of LABs and SMGs. The rectangular box represents the region Pope et al. (2008) identified as the location of sources starburst dominated in the mid-infrared. The higher 8 μm/4.5 μm flux ratios are generally only obtainable by AGN, as only their SEDs should be that steep at these high redshifts ($z > 2$). Submillimeter sources with similar redshifts to the LABs in this study, taken from Pope et al. (2006), have very similar 24 μm/8 μm and 8 μm/4.5 μm flux ratios, with mean colors that are the same, to within one standard deviation, as that of the LAB counterparts presented in Figure 1.

For comparison, we overplot a series of models derived from Chary & Elbaz (2001, hereafter CE01). As CE01 is based on low-redshift infrared galaxies, we applied an evolution in specific star formation to account for the expected buildup of stellar mass with time, a factor of $(1+z)^2$. This redshift evolution roughly matches the evolution in integrated specific star

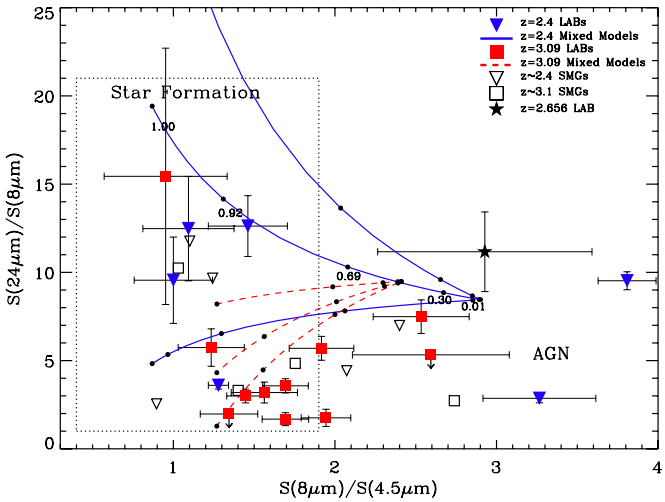

Figure 1. 8 μm/4.5 μm ratio vs. 24 μm/8 μm ratio for our sample of LABs (solid symbols). Triangle (blue) symbols are $z = 2.4$ sources, squares (red) are $z = 3.1$, and the star is LAB1_J1434+3317 at $z = 2.66$. For comparison, we also plot the submillimeter galaxies (SMGs) at similar redshifts from Pope et al. (2006) as hollow symbols. The lines are models derived from Chary & Elbaz (2001), running from star formation dominated on the left to AGN dominated on the right. The solid lines are $z = 2.4$ (blue) models, while the dotted lines are $z = 3.1$ (red). The rectangular box is taken from a similar plot of submillimeter galaxies from Pope et al. (2008), marking the likely location of galaxies powered by star formation.

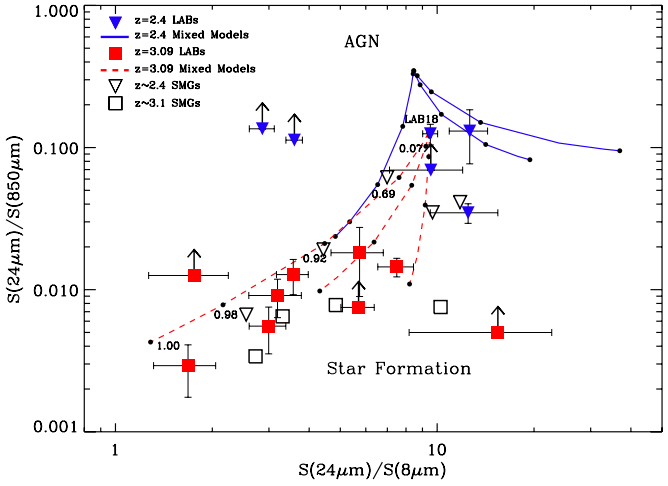

Figure 2. 24 μm/850 μm ratio vs. 24 μm/8 μm ratio for our sample of LABs (solid symbols). Triangle (blue) symbols are $z = 2.4$ sources, while squares (red) are $z = 3.1$. For comparison, we also plot the SMGs at similar redshifts from Pope et al. (2006) as hollow symbols. The model lines are the same as in Figure 1, now running from star formation dominated on the bottom up to AGN dominated on the top. All of the submillimeter-detected LABs plotted appear to lie at the locus of star formation.

formation found for the massive galaxies studied by Papovich et al. (2006), erring on the side of more conservative (i.e., less) evolution. Stronger evolution in specific star formation would produce larger 24 μm/8 μm ratios, moving the star formation ends of all the models upward on the plot.

The CE01 models cover a range in luminosity, so we selected three that are representative of that entire range. Changing exactly which models are plotted makes no difference to the results or discussion we present here. Finally, we mixed the star-forming CE01 SED models with the SED of an AGN (Mrk 231) to produce a range of ratios from AGN to star formation dominated. On the plot the models start to the left and/or high above as pure star formation and converge on pure Mrk 231 around 8 μm/4.5 μm $\sim$2. The $z = 2.4$ models (solid lines) cover a much larger range in 24 μm/8 μm ratio than the $z = 3.1$ models (dotted lines) because of the possible presence of the large 7.7 μm PAH feature at that redshift.

Nearly two thirds (59%; 10 of 17) of the LAB-associated sources fall within the star formation rectangle, 29% have mid-infrared colors clearly indicative of AGN, while the two remaining sources (12%) are borderline, but likely also contain significant AGN contribution. On the surface, this would indicate that the majority of sources associated with LABs are powered by starbursts. However, even an AGN dominant in the infrared can still have significant contribution from stars at rest wavelength 1 μm which has the effect of flattening its slope considerably, i.e., it decreases the 8 μm/4.5 μm ratio. For instance, the Mrk 231 ratios presented here (the converging end point of the models we plot in Figure 1) differ somewhat from the Mrk 231 model ratios presented in Pope et al. (2008), particularly at $z \sim 3$. This is likely a result of their use of an Mrk 231 model based only on mid-infrared data (a Rigopoulou et al. (1999) mid-infrared spectrum combined with a fit to *Infrared Astronomical Satellite* photometry). The Mrk 231 model we use comes from a multi-component fit (Armus et al. 2007) that includes the critical stellar component fit to near-infrared data points, which has a strong effect on the resulting 8 μm/4.5 μm ratio at $z > 2$.

In addition, at these redshifts these ratios are extremely sensitive to hot dust, which one would expect to be dominated by any AGN, even if the AGN was not a significant contributor to the total infrared luminosity. Alternatively, an extreme starburst can also produce a large amount of emission from hot dust, which could produce similar IRAC colors to an AGN (Yun et al. 2008). This diagnostic plot makes no direct measurement of the far infrared luminosity, the source of which we are trying to determine.

4.2. Mid-IR to Submillimeter Ratios

At the redshifts of LABs with submillimeter imaging ($z = 2.4$–3.1), 850 μm is sensitive to rest wavelength 200–250 μm, past the peak of far infrared cold dust emission, where flux density is beginning to fall like a Rayleigh–Jeans law ($F_\nu \propto \nu^2$). *Spitzer* MIPS 24 μm observations are sensitive to the rest-wavelength 6–7 μm mid-infrared, blueward of the far-infrared peak and very sensitive to both hot dust and the presence of PAHs (although less so for PAHs at the higher redshift, see discussion below). *Spitzer* IRAC observations at these redshifts are not very sensitive to dust emission but instead can be dominated by stellar emission. In particular, 8 μm is roughly equivalent to the rest-wavelength *K* band, an excellent tracer of total stellar mass.

The combination of *Spitzer* mid-infrared with submillimeter flux densities, each being sensitive to a different temperature regime (stars, hot dust, cold dust), can do a great deal to reveal the likely power sources of the infrared-bright galaxies within the blobs. In particular, a simple color–color plot (ratio of MIPS 24 μm to 850 μm submillimeter versus ratio of MIPS 24 μm to IRAC 8 μm) can be a powerful tool for discriminating AGN from star formation, as well as getting a picture of the specific star formation (star formation rate (SFR) per unit mass).

In Figure 2, we plot the 24 μm/850 μm ratio versus the 24 μm/8 μm ratio for the three fields listed above that have both blobs and deep submillimeter coverage. Any source without a 24 μm detection is not plotted. In the case of LAB6_J2143−4423, there are two MIPS 24 μm

sources with confirmed $z = 2.38$ redshifts (Scarlata et al. 2009), so both sources (LAB6a and LAB6b) are included on the plot, but the submillimeter detection has been assigned to LAB6b_J2143−4423 (as described above). Similarly, LAB1_J2217+0017 is associated with two equally bright 8 μm sources (LAB1a and LAB1b). Due to the large submillimeter beam size, it is not possible to deduce which source is likely associated with the 850 μm flux and, of course, both may be. We have therefore combined the 8 μm and 24 μm fluxes of LAB1a_J2217+0017 and LAB1b_J2217+0017 into a single source for the purpose of this plot. If all the submillimeter flux were to originate in the slightly fainter 24 μm source (LAB1a_J2217+0017), the 24 μm/850 μm ratio would go down by an additional factor of three, with very little change in 24/8 μm.

We overplot the same CE01/Mrk231 mixed models as used in Figure 1. We marked the ratio of star formation luminosity to AGN luminosity for one of the models, running from 1.0 (100% starburst) upward to 0.0 (100% AGN) contribution from star formation to the total bolometric luminosity.

All eight of the submillimeter detected components for LABs have mid-IR/submillimeter ratios consistent with star formation. An additional six of the LAB components are only upper limits, but only two of those (LAB6a_J2143−4423 and LAB19_J1714+5015) are clearly outside and above the locus of star formation, consistent with the IRS spectrum of LAB6a_J2143−4423 (see below; Scarlata et al. 2009) and the broad-line nature of LAB19_J1714+5015 (Pascarelle et al. 1996; Colbert et al. 2006a). This submillimeter evidence for significant quantities of cool dust in LABs was previously noted by Webb et al. (2009), who found that all but one of the SSA22 8 μm sources they studied were detected at 850 μm as well. That strong trend does not hold true for our sample, where 6 of 14 of our LAB counterparts are detected at 8 μm but not at 850 μm, but that could be at least partially attributable to the slightly different depths and redshifts in our study.

This plot strongly indicates that the majority of these infrared-bright components of LABs are not powered by AGN alone, but there are two important caveats. First, the present sensitivity limits of submillimeter surveys are just barely deep enough to conduct this experiment. Not only are nearly half the sources not detected at all, but none of the actual detections are that strong, ranging from 2.5σ to 8σ, with half of 4σ significance or less. Fortunately, the expected range of the 24 μm/850 μm ratio is large, especially at $z = 3.1$, allowing for a strong discrimination even with very large submillimeter errors.

Second, while the correction for mass evolution is likely generally correct, it is almost certain that there will be real variations in specific star formation history from galaxy to galaxy. On the plot this will move galaxies back and forth horizontally, which will change what models and AGN/star formation percentage one would associate with it. This is not an important effect at $z = 3.1$, where the models are less degenerative and there is large separation in the 24 μm/850 μm ratio as the AGN contribution is increased, but it can be a concern at $z = 2.4$. The mid-IR to submillimeter ratios at the $z = 2.4$ are not as strong for discriminating the energy source because of the presence of the powerful PAHs in the 24 μm filter, which can somewhat mimic the rising power-law slope of an AGN.

For instance, LAB18_J1714+5015 (labeled in Figure 2) appears to lie roughly in the neighborhood of the 93%–98% star formation models. However, a change in the specific star formation of the nearby models by 30% would shift it toward the AGN models such that it would only take a factor of ∼2–3 change in the 24 μm/850 μm ratio (either the model or through a measurement error) to make this source AGN dominated. In fact, its IRS spectrum (see below) suggests that it is completely AGN dominated. To similarly shift $z = 3.1$ sources would require changes of factors of 10–20 in the 24 μm/850 μm ratio.

For further comparison, we also plot SMGs spectroscopically confirmed at similar (±5% in 1 + z) redshifts from Pope et al. (2006). The mid-infrared colors and mid-infrared to submillimeter ratios for the Pope et al. (2006) SMGs are very similar to those from the LAB sample, with the exception of one $z \sim 2.4$ submillimeter source (GN22) with a 24 μm/850 μm color so cool it cannot be easily explained by our simple set of models. Three of these $z \sim 2.4$ SMGs also have IRS mid-infrared spectroscopy (GN04, GN05, and GN19; Pope et al. 2008). All three have significant PAH features, despite the fact that two of the three are detected in the hard X-rays. Looking at the line-to-continuum (L/C) ratios, Pope et al. (2008) found that only GN04 (the source with the largest 24 μm/850 μm ratio included from their study) had >50% contribution to the mid-infrared energy output and they classified it as a mixed (AGN + starburst) source.

We note that one blob in our sample falls on the low end of the models. This is the $z = 3.09$ (Steidel et al. 2000) LAB1_J2217+0017, which has a large reported submillimeter flux (16.8 ± 2.9; Chapman et al. 2004), but is quite faint at 24 μm with a flux of only 71 ± 7 μJy. This is actually the combined 24 μm flux of the two bright 8 μm sources identified at this location (Webb et al. 2009; Geach et al. 2007). If split back into their two components, the 24 μm fluxes are 25 and 47 μJy, so if the submillimeter flux came from just one of them the 24 μm/850 μm ratio would be even more extreme. LAB1_J2217+0017 was undetected in high spatial resolution observations (∼2″) taken with the SMA (Matsuda et al. 2007), indicating that the 850 μm flux must be widely spread out or split into multiple sources. Alternatively, the original measurement might be a several sigma deviation. ASTE-AzTEC 1.1 mm observations failed to detect it down to 10 mJy (Kohno et al. 2008). However, even a factor of 10 less flux would still place LAB1_J2217+0017 in the region dominated by star formation.

4.3. PAH Features in LAB ULIRGs

Of the six sources associated with LABs targeted with IRS spectroscopy, four show significant PAH features. In order to measure individual PAH emission lines, we used the IDL PAHFIT software package (Smith et al. 2007), which fits all PAH emission lines and continuum simultaneously. Given the limited coverage of the data, we only include the PAH lines in the fit that cover the wavelength range of interest (6–9 μm) and a single red continuum. We chose this over the more direct method of isolating the region directly around each line of interest and fitting a line and continuum there (i.e., Pope et al. 2008), as that can underestimate the equivalent widths (EWs) by factors of up to four. Fits to all six spectra are shown in Figure 3 and all fluxes, EWs, and L/C ratios are listed in Table 3.

Two of the spectra show no apparent PAH features, with all line fits producing fluxes below the 1σ uncertainty. These featureless sources are the counterpart LAB6a_J2143−4423 (previously reported in Scarlata et al. 2009) and LAB18_J1714+5015 (Keel et al. 1999).

The remaining four sources all show the 7–9 μm PAH complex (∼7.4–8.7 μm) at the expected location for their redshifts.

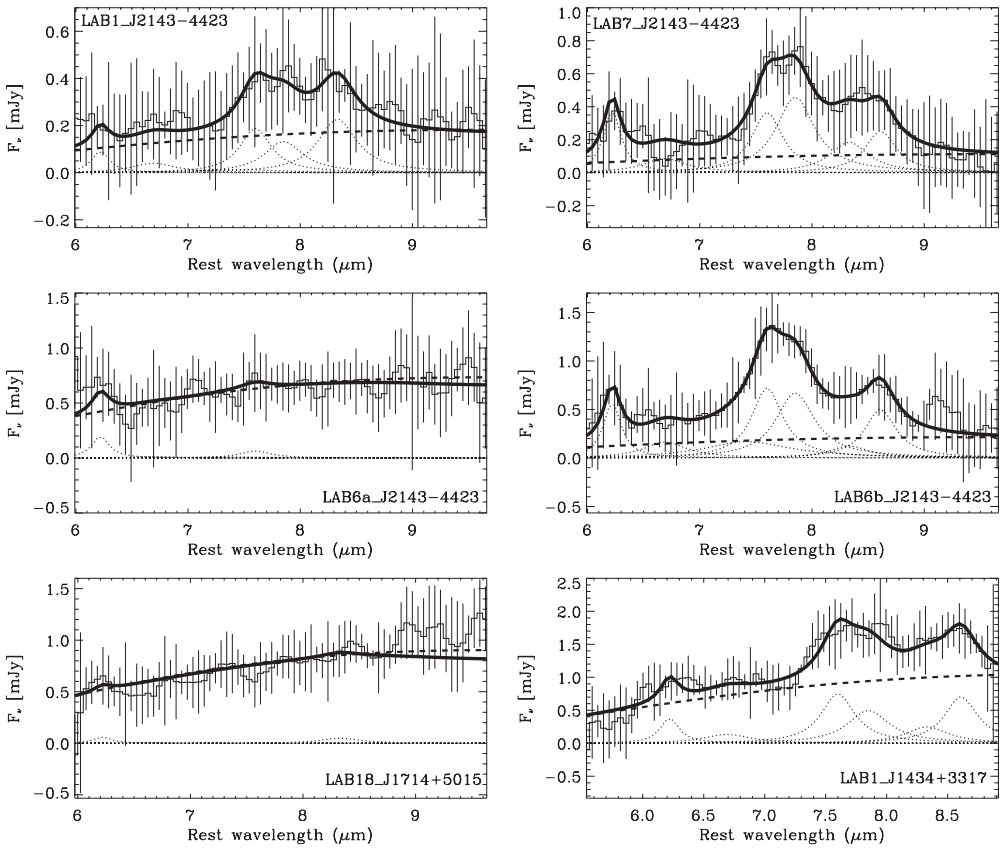

Figure 3. IRS spectra of six MIPS-detected LABs. Figures show the best continuum (dashed line) and PAH fits (dotted lines) as determined by PAHFIT. The combined fits (PAHs + continuum) are the thick solid lines overlaid on the data.

Table 3
Lyα Blob PAH Characteristics

Name	6.2 μm Flux (10^{-15} erg cm^{-2} s^{-1})	7.7 μm Flux (10^{-15} erg cm^{-2} s^{-1})	6.2 μm Lum (10^{10} $L_\odot$)	7.7 μm Lum (10^{10} $L_\odot$)	L/C Ratio	SFR ($M_\odot$ yr^{-1})
LAB1_J2143−4423	0.55 ± 0.46	2.64 ± 1.5	0.63	3.0	1.5 ± 0.7	420
LAB6a_J2143−4423	<1.3	<0.9	< 1.5	< 1.3	<0.14	<130
LAB6b_J2143−4423	3.2 ± 0.9	11.8 ± 2.0	3.6	13.4	4.8 ± 1.4	2000
LAB7_J2143−4423	2.23 ± 0.7	6.9 ± 1.6	2.6	8.0	6.1 ± 3.4	1200
LAB18_J1714+5015	<1.2	<0.9	< 1.3	< 1.3	<0.11	<140
LAB1_J1434+3317	2.25 ± 0.9	9.5 ± 2.3	3.4	14.3	0.81 ± 0.16	2200

The weakest PAH detection is that of source LAB1_J2143-4423, with a 7.7 μm feature (defined as the combination of the 7.60 and 7.85 μm PAH lines) detection of only 2σ significance. However, the whole 7–9 μm complex for the LAB1_J2143−4423 source is detected at 4σ significance. Combined with their discovery at the appropriate wavelengths, there is little doubt that the PAH features for LAB1_J2143−4423 are real.

We measured a 7.7 μm L/C ratio for each source in order to test the contribution of any possible AGN to the total infrared energy output. For ease of comparison, we use the same method of Rigopoulou et al. (1999), taking the average intensity of the line and continuum over 7.57–7.94 μm. The error in line intensity is just a quadratic sum of uncertainty in the data, but the error in continuum is dominated by the quality of the continuum fit, which has only two parameters, temperature and a normalization factor, for each of which the fitting routine returns an uncertainty. Using a Monte Carlo method, we take the two derived probability distributions of temperature and normalization factors to create a large distribution of average continuum intensities from which we measure a final rms. This continuum error is consistently large, often dominating the error in L/C.

Using their L/C definition, Rigopoulou et al. (1999) found that AGNs have L/C $\simeq$ 0.2, pure starbursts have L/C $\simeq$ 3, and the typical local ULIRGs have L/C $\simeq$ 2, indicating that they are almost completely star formation dominated. The two sources from our survey with no detected PAH features have L/C ratios $<$ 0.2–0.3 (2σ limits), clearly AGN-dominated sources. The two with the most powerful PAHs have L/C = 5–6. Even accounting for large errors in L/C (the LAB7_J2143−4423 error is $\sim$50%), it is clear that these are star-formation-dominated sources. The final two sources are a bit less clear. With an L/C of 0.8 ± 0.2, LAB1_J1434+3317 appears to have its main mid-IR contribution from an AGN, but the star formation component is far from negligible. For LAB1_J2143−4423, its L/C (1.5 ± 0.7) suggests a similar but opposite situation: the primary contribution

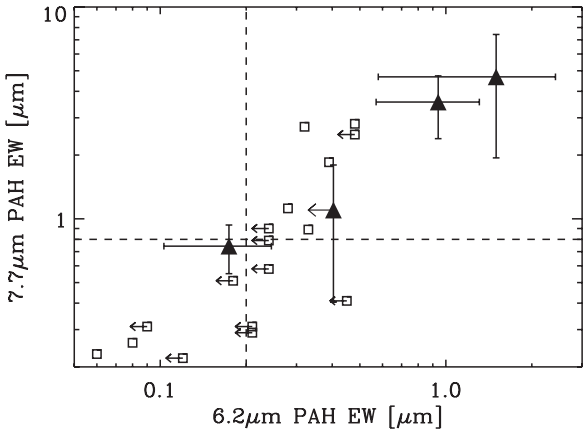

Figure 4. 6.2 μm PAH EW vs. 7.7 μm PAH EW. The square points are high-z ULIRGs from Sajina et al. (2007). The dotted lines at 6.2 μm EW = 0.2 μm and 7.7 μm EW = 0.8 approximate a cutoff between AGN and star-formation-dominated sources.

is from star formation, but the AGN component is significant. The large error on the LAB1_J2143−4423 L/C does add some further confusion, as a 1σ deviation could easily change the likely power source.

Another similar way to approach this problem is to look at the PAH EWs. We plot the 6.2 μm EW versus the 7.7 μm EW in Figure 4. The 6.2 μm feature is less contaminated by nearby PAHs and silicate absorption and therefore can be less vulnerable to the continuum model chosen. Unfortunately, for most of our data the 6.2 μm feature lies near the noisier wavelength edge of the LL1 IRS detector, limiting the information available for the continuum there. The 6.2 μm PAH was also not always strongly detected for similar reasons. In the case of LAB1_J2143−4423, the 6.2 μm PAH emission is undetected, so instead we plot a 2σ upper limit.

EWs of PAHs are extremely vulnerable to how the exact line fitting is done, as they are a combination of both the line measured and continuum fit assumed. A factor of two difference in measured fluxes can easily result in a factor of four difference in EW. This can make it problematic to compare EWs between studies that have not approached the measurement in a similar way. We therefore compare our four PAH-detected sources to the $z = 1$–3 ULIRGs of Sajina et al. (2007), where they also applied a multi-component PAH profile fit. Some differences remain, as Sajina et al. (2007) covered a longer range of wavelengths, which produces somewhat different continuum fits. Our fits seem to be favoring a continuum that is slightly lower, leading to slightly larger EWs. However, considering the large errors, the two methods produce similar results.

The dashed lines on the figure (6.2 μm EW = 0.2 μm and 7.7 μm EW = 0.8 μm) are also from Sajina et al. (2007) and represent suggested dividing lines between strong-PAH (i.e., star forming) and weak-PAH sources (i.e., AGN-like). Only 25% of the Sajina et al. (2007) high-z ULIRG sample fell into the strong PAH (they are half the sources on the plot, but that is misleading as 7.7 μm limit-only objects are not plotted), as opposed to half of our sample (our two PAH-free sources are not plotted). While the lines are mainly a device to assist comparison between studies, they do appear to be in rough agreement with what we found looking at 7.7 μm L/C ratios.

Star formation rates can be derived from PAH luminosities (i.e., Chary & Elbaz 2001; Brandl et al. 2006), although the uncertainties and unknowns increase with redshift and luminosity. Using the 7.7 μm to total infrared luminosity formulae suggested by Pope et al. (2008) for their sample of SMGs, we derive star formation rates and/or limits for our six sources (see Table 3). As already discussed above, our method of fitting all PAH features and continuum simultaneously produces larger PAH fluxes than if one just fit a continuum locally around each PAH emission feature, as Pope et al. (2008) did for their sample. Therefore, if we simply put our derived luminosities into the Pope et al. (2008) formulae, we would certainly be overestimating the star formation rate. For our 4 detected 7.7 μm emission features, we found a mean correction factor to our fluxes of 1.7 if we use a method similar to that of Pope et al. (2008). We apply this correction, dividing the 7.7 μm luminosities in Table 3 by a factor of 1.7, before applying the formulae of Pope et al. (2008).

We find star formation rates in our PAH-detected sample ranging from 420 to 2200 $M_\odot$ yr^{-1}, significantly larger than the limits we found for our two non-PAH sources which were $<$130–140 $M_\odot$ yr^{-1}. While these rates are derived from the 7.7 μm fluxes, the 6.2 μm feature can also be used to derive total infrared luminosity and, consequently, SFR. While our 6.2 μm feature detections are generally quite weak, the star formation rates derived from them agree with those from 7.7 μm within the errors. The most discrepant source is that of LAB1_J1434+3317, which despite having a low L/C ratio does have the brightest 7.7 μm luminosity of the sample. While technically within the errors, its 6.2 μm luminosity points toward an SFR closer to 1000 $M_\odot$ yr^{-1}. None of the other 6.2 μm SFR estimates are off by more than a few hundred $M_\odot$ yr^{-1}. This could be due to LAB1_J1434+3317 being such a strongly mixed (starburst and AGN) source or perhaps because it is such a highly luminous mid-infrared source. Both are known to affect conversion from PAH luminosity to far infrared luminosity (Murphy et al. 2009).

We can then ask the question whether these star formation rates are enough to power the LABs. Star formation might cause the LABs in two different ways: photoionization from Lyman continuum photons escaping from the galaxy and supernova-driven outflows into the surrounding medium, producing shocks.

For photoionization, we can estimate the number of ionizing photons produced from the Bruzual & Charlot (2003) models which use a high-mass cutoff of 100 $M_\odot$. Assuming an age greater than 15 Myr (after which the number of ionizing photons produced by continuous star formation become roughly constant), for every 1 $M_\odot$ yr^{-1} the young stars will generate $\sim 9 \times 10^{52}$ ionizing photons s^{-1}. The predicted Lyα luminosity is therefore

$$L_{\mathrm{Ly}\alpha} = 0.6 f_{\mathrm{esc}} h\nu \times [\mathrm{SFR}] \times (9 \times 10^{52}) \ \mathrm{erg\ s^{-1}},$$

where $h\nu$ for Lyα is 2.58×10^{-12} erg, 0.6 is the fraction of absorbed Lyman continuum photons that will be re-emitted as Lyα photons, and f_{esc} is the fraction of Lyman continuum photons that can escape from the galaxy. For an SFR of 1000 $M_\odot$ yr^{-1}, we predict $1.4 \times 10^{44} f_{\mathrm{esc}}$ erg s^{-1}. For f_{esc} near unity one could power most blobs with the ionizing continuum from the starbursts, but such a high escape fraction for the Lyman continuum is highly improbable for these sources where most of the energy is coming out as reprocessed dust emission. The majority of rest-frame ultraviolet photons are certainly not escaping along our line of sight. If we apply a more conservative $f_{\mathrm{esc}} = 0.1$ then there are not enough ionizing photons from star formation escaping to produce any of the LABs with PAH-emitting sources presented here, with deficits ranging from factors of 2–13.

For supernova-driven outflows, we start by estimating the number of supernovae generated per year. Again using the Bruzual & Charlot (2003) models, we estimate 5×10^{-3} SN per $M_\odot$ yr^{-1}. If each supernova produces $\sim 10^{51}$ erg, then star formation is generating roughly 1.7×10^{41} erg s^{-1} for every $M_\odot$ yr^{-1}. This is enough energy to power the LABs, but we still have to account for the efficiency of the conversion of the supernova energy into kinetic outflows. Thornton et al. (1998) indicate that as much as 70%–90% of the supernova energy will be radiated away, leaving only $(1–3) \times 10^{50}$ erg of kinetic energy remaining. If we account for this efficiency, our typical 1000 $M_\odot$ yr^{-1} infrared LAB counterpart will generate $(2–5) \times 10^{43}$ erg s^{-1}. Except for the most pessimistic assumptions, there appears to be enough supernova energy available to power two of the three star-formation-dominated LABs, with only LAB1_J2143−4423 falling short by nearly a factor of four. We note that a more top heavy initial mass function (IMF) with larger mass upper limits will produce both more supernovae and ionizing photons. While this will certainly produce more Lyα photons, it is unlikely the IMF could be radically different enough from our assumptions to change the results. So, while star formation cannot produce enough ionizing photons to generate LABs, there is enough energy in supernova outflows to do so, but not in every case.

The requirement for detection at 24 μm clearly has the potential to introduce a bias into our analysis. Without a powerful 7.7 μm feature, the 24 μm flux of $z = 2.4$ sources would generally be less, likely removing it from this sample (>0.2 mJy) altogether. One known $z \sim 2.4$ LAB, LAB19_J1714+5015 (Keel et al. 1999), was excluded because its 24 μm flux density is not above ∼0.2 mJy, just missing our cut. It is a known broad-line AGN (Pascarelle et al. 1996; Colbert et al. 2006a) which likely dominates its mid-infrared output. However, that is the only 24 μm observed LAB at redshift $z < 3$ known at the time of our program that was not observed by IRS. Unfortunately, the number of known LABs at redshifts below $z = 3$ remain very small (roughly a dozen), so we must not draw too many conclusions from such a small sample. Of those galaxies associated with LABs that are bright at 24 μm, half have strong PAHs and appear to be star formation dominated.

None of the LABs in the higher redshift $z = 3.09$ SSA22 field had bright 24 μm fluxes, but at their redshift the powerful 7.7 μm PAH feature moves beyond the MIPS 24 μm filter which instead becomes sensitive to the continuum below 6 μm. That is a region of the spectrum of galaxies that is generally dominated by hot dust, meaning at this higher redshift one might expect a reverse of the selection bias: brighter 24 μm will indicate a stronger hot dust component, i.e., a greater contribution from AGN. Four of the five SSA22 blobs (80%) with luminous X-ray counterparts (Geach et al. 2009) are detected at 24 μm (40–160 μJy), as opposed to the remaining 10 non X-ray luminous sources observed with MIPS 24 μm, for which only four (40%) are detected (50–80 μJy).

We wish to provide one final word of caution on the use of PAH flux to continuum ratios for trying to breakdown the total bolometric output for such powerful, high-redshift objects. It is entirely possible that star-forming galaxies, forming at rates of more than 1000 $M_\odot$ yr^{-1} might produce significant quantities of hot dust emission without AGN (i.e., Hunt et al. 2002) and/or produce conditions that destroy the grains that produce PAHs (i.e., Galliano et al. 2003). However, the continued discovery of PAHs in bright, high-z sources (i.e., Fadda et al. 2010; Huang et al. 2009; Yan et al. 2007) suggests the issue of PAH destruction is likely not a serious problem. If anything, there appears to be evidence that the brightest, high-redshift galaxies are overproducing PAH emission compared to their lower redshift, less luminous counterparts (Murphy et al. 2009).

Whether we measure *Spitzer* photometry ratios, compare mid-infrared to submillimeter fluxes, or examine the strength of PAHs using IRS spectroscopy, we consistently find a very similar answer: half to 2/3 of all LAB counterparts appear to have their infrared luminosity powered mainly by star formation. This does not prevent powerful AGN from also existing within these sources or rule AGN out as a source of the extended Lyα emission. However, with such large reservoirs of starburst energy it does make star formation-driven LAB models, such as superwind outflows, a much more likely power source for the majority of LABs.

4.4. Blob Counterpart Masses

Several lines of evidence suggest that LABs mark the regions of massive galaxy assembly: their location at the peak of high-redshift structures (Matsuda et al. 2009, 2004; Palunas et al. 2004), their number densities comparable to galaxy clusters in the nearby and high-z universe (10^{-5}–10^{-6} Mpc^{-3}; Yang et al. 2009), the frequent indicators of merger and/or interaction (Colbert et al. 2006b; Chapman et al. 2004; Francis et al. 2001). One possibility is that they could be a phase in the formation process of massive elliptical galaxies themselves. *Spitzer* IRAC data provide us with rest-wavelength measurements of the 1–2 μm portion of the SED of the infrared components of the LABs being analyzed in this paper. This is ideal for estimates of mass, lying at the peak of stellar light output while minimizing the effects of dust extinction.

However, the mass-to-light ratio (M/L) can change significantly, even at these wavelengths, for the young objects that one expects to find in the early universe. Robust mass estimates require a good age estimate, so therefore most studies perform a full SED fit to estimate the age in order to derive an M/L ratio and total mass.

Previous measurements of LAB counterpart masses regularly find the brighter LABs to be around 10^{11} $M_\odot$ (Geach et al. 2007; Smith et al. 2008). Uchimoto et al. (2008) measured masses for seven SSA22 LABs, deriving masses from their K-band data ranging from 4×10^9 to 1.1×10^{11} $M_\odot$, which they found to be roughly correlated with the luminosity of the LABs within which they resided. In addition, both LAB1_J2143−4423 (Francis et al. 2001) and LAB6b_J2143−4423 (Scarlata et al. 2009) have undergone a full SED fitting analysis, producing masses of $\sim 1.5 \times 10^{11}$ $M_\odot$ and 4×10^{11} $M_\odot$, respectively. In the case of LAB1_J2143−4423, there were two fits done, one to each major component, but as we are unable to resolve the two components in the coarser IRAC data used in this study we report only the combined mass here.

A full SED fitting is not possible for all galaxies associated with the LABs, due to the paucity of the some of the necessary deep data—especially the near-infrared—for the different fields. For instance, the 4000 Å break, one of the more critical features for age estimation, lies entirely in the near-infrared at the redshifts of the LABs. More importantly, even with full spectral coverage, SED fits can suffer from AGN contamination and age/dust extinction degeneracy, both of which will strongly affect any mass determination. Even measurements of the 4000 Å break, which are robust for measuring the age of older populations, will fail to provide accurate ages for young starbursts, like those likely present at the high energies and

early universe epoch we are studying. We therefore decided to examine the mass upper limits for our LAB counterparts.

Almost all of the galaxies in our study are covered with the four IRAC channels, covering the rest frame 1.1 μm both at $z = 3.1$ and at $z = 2.4$. We convert the 1.1 μm luminosity to stellar masses assuming a simple single stellar population model (Bruzual & Charlot 2003) with no dust. In order to compare galaxies at different redshifts, we have computed maximally old stellar population models at the observation redshift, assuming $z = 8$ formation redshift. The derived masses, therefore, provide an upper limit to the real stellar masses, since they are computed under the assumption that all the 1.1 μm luminosity is due to old stars. To give an idea how much this could overestimate the masses, we can compare to the SED model fit done for the X-ray-detected LABs in SSA22 of Geach et al. (2009). They found that a relatively young SED model with 100 Myr of continuous star formation history and an extinction of $A_V = 1.5$ was the best fit for their X-ray emitting sources. If this same model applied to all the LAB counterparts, their masses would be lower by a factor of 5.7 at $z = 3$ and 6.7 at $z = 2.4$ than our plotted maximum mass limits. However, for the cases of a couple of our brighter sources (LAB1_J2143−4423 and LAB6b_J2143−4423) the upper limits are within a factor of ∼2 of the masses previously derived from a full SED fit (Scarlata et al. 2009; Francis et al. 2001). Of the SSA22 LAB counterparts included in both our study and that of the *K*-band study of Uchimoto et al. (2008), the typical difference is a factor of ∼2–2.5, although two sources have very large disparities (LAB7_J2217+0017 and LAB16_J2217+0017), for which the difference is closer to a factor of 8–10. The 4.5 μm/8 μm ratio of LAB16_J2217+0017 suggests that it may contain an AGN, so these may be examples of AGN contamination. LAB7_J2217+0017 is too faint to apply any of our infrared AGN/starburst diagnostic ratios.

An analysis using these mass upper limits has another advantage. If the LAB components are all of similar formation era, whatever that may be, then they should have very similar 1.1 μm M/L ratios and their masses *relative* to one another would be accurate no matter when exactly they all formed.

We plot these mass upper limits versus the Lyα luminosity of the blob within which they are found in Figure 5. The errors plotted are just from the photometry and do not represent the significant uncertainties resulting from the model M/L ratios, choice of formation redshift, etc. In the cases of more than one mid-infrared source (LAB1_J2217+0017 and LAB6_J2143−4423), both are plotted with the same Lyα luminosity. The clearest result is that there are no low mass, high Lyα luminosity sources. In fact, one could split the blobs into two groups: a Lyα bright ($>2 \times 10^{43}$ erg s^{-1}), high-mass sample, and a Lyα faint ($<2 \times 10^{43}$ erg s^{-1}) sample with no strong preference for mass which does not quite reach the most massive end of the LAB sample. This lack of Lyα bright, low-mass sources would continue to hold true even if one were to reduce the masses of the bright Lyα sources by the factor of ∼6 suggested for the Geach et al. (2009) X-ray LABS, while leaving the masses of the Lyα faint sources unchanged. The limited mass fitting by ourselves and previous studies (i.e., Uchimoto et al. 2008) suggest that if there is any systematic difference in the M/L ratio with Lyα flux, it is actually the Lyα bright sources that tend to have higher M/L, which would make this split stronger.

This possible split is similar to the two populations proposed by Webb et al. (2009), infrared luminous and infrared faint,

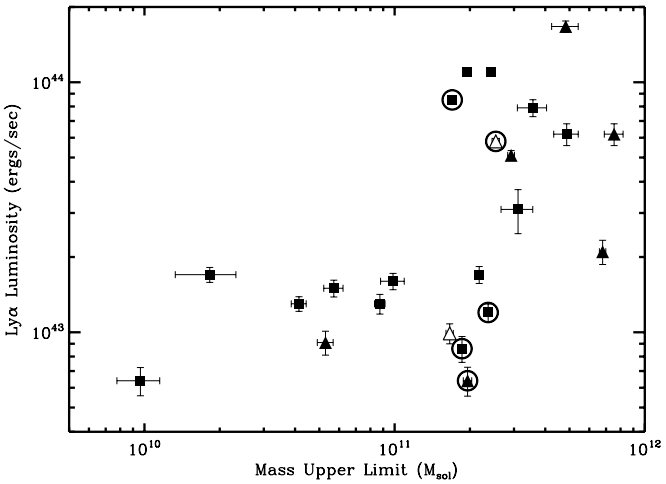

Figure 5. Plot of mass upper limits vs. Lyα luminosity for the associated blob. Blob components with AGN *Spitzer* colors are plotted as solid triangles while the two with borderline 8 μm/4.5 μm colors are plotted as empty triangles. The X-ray-detected blobs are circled.

which they based mainly on whether the counterpart possessed an 8 μm detection. Their conclusion that the infrared luminous LAB counterparts had large hot dust contributions from AGN and/or intense starburst ULIRG activity while the infrared faint counterparts resembled cooler, pure star formation systems, does not appear to apply as well to Lyα luminosity or mass. Our plotted sample shows evidence for AGN contribution throughout the entire range of Lyα luminosity studied and all but the faintest end of the mass limits. However, the Webb et al. (2009) study does include the smallest and faintest of the SSA22 blobs which we removed from our study.

The presence of a bright AGN would contaminate the rest wavelength 1.1 μm and produce masses much higher than are actually present in stars. We have marked all those sources with IRAC colors indicating AGN (this includes our three AGN-dominated IRS spectra) with solid triangles. We also mark the two borderline AGN cases from Figure 1 with empty triangles. Finally, we circle all the X-ray-detected blob counterparts from Geach et al. (2009). If these potential contaminant LABs were removed from the sample, a weak trend appears with the most massive sources associated with the brightest Lyα luminosities. However, with only ∼10 sources and the general uncertainties in both AGN contamination and actual mass this trend is far from confirmed.

While it is unlikely that the masses of these mid-infrared components all lie at their upper limits, it is clear many are quite large, around 10^{11} $M_\odot$. Massive galaxies with substantial (>0.5 Gyr) ages are not unusual at these redshifts (Kriek et al. 2008). Some of our largest masses could be a combination of a close pair, like those known to be in LAB1_J2143−4423 (Francis et al. 2001). In another case, LAB1_J2217+0017, the two sources are barely distinguishable at the IRAC resolution, so it would not be that surprising to find others that could not be. Whether a single galaxy or some sort of merging/interacting pair (or more), the total mass of all the galaxies is likely indicative of the size of the potential well in which the galaxy is assembling. The weak correlation of mass and Lyα luminosity, if real, would indicate a correlation between the size of this potential well and the energy source that is powering the blob. If the LAB is a cooling flow, one would expect a direct correlation of potential well to Lyα luminosity, but that does not rule out stellar wind or AGN illumination models, as a greater potential well might

be expected to drive more gas inflow causing star formation or feeding a supermassive black hole.

5. SUMMARY AND CONCLUSIONS

Mid-infrared *Spitzer* ratios (rest frame near- and mid-IR) indicate that ∼60% of LAB counterparts are consistent with being cool starbursts, while the rest have a substantial hot dust component that one would expect from an AGN, although extreme starbursts are a possibility in some cases. Including submillimeter observations (rest-frame far infrared) in the analysis produces a similar conclusion: roughly 2/3 of LAB counterparts are consistent with the total bolometric energy output being dominated by star formation.

IRS spectroscopy of six of the brighter (and lower redshift) sources found four of six to have measurable PAHs. The other two were featureless power-law spectra indicative of AGN domination. Of the four detected, two had L/C ratios and PAH EWs suggestive of mixed sources, with energy contributions from both star formation and supermassive black hole accretion.

In general, the stellar masses of the LAB counterparts are quite large, around $10^{11}\ M_{\odot}$. There is a weak trend with the Lyα luminosity of the host blob. This could be suggestive of two populations of LAB: one Lyα luminous and generally massive and one fainter and slightly less massive, but generally covering a wide range of stellar masses. Alternatively, the LAB counterparts could be one continuous population, with mass growing with Lyα luminosity. Indications of AGN are seen at all Lyα luminosities and all but the smallest masses.

A lot of the work on LABs has been spent trying to determine the energy source that powers them. Not only would that allow us to understand the physics of these giant clouds of extended Lyα emission, but could possibly provide valuable information on the assembly of massive galaxies, including questions of AGN feedback, escaping ionizing radiation, and/or cooling flows. It has been theorized that LABs could be a short-lived evolutionary step in the life of most galaxies at these redshifts (Geach et al. 2009). The Lyα halo could be powered by star formation superwinds, growing larger and larger until the central AGN grows enough to blow out most of the gas and cutting off the LAB's power source (Webb et al. 2009).

The problem with trying to place all the observed LABs in an evolutionary sequence is that again and again the blobs resist efforts to link them to a single power source. While Geach et al. (2009) found that five LABs were strong X-ray sources, their further submillimeter analysis suggested that even for these objects, the total bolometric output for the galaxy is dominated by star formation. The presence of AGN, seen in many LABs, could just be confusing the analysis or maybe indicating a future evolutionary stage. Our own analysis of submillimeter and mid-infrared data suggests a great deal of the LAB infrared counterparts show no indication of a significant hot dust component, again pointing toward star formation, but there are several significant exceptions.

The IRS spectra from this study reveal two LAB infrared counterparts each with an unambiguous, featureless AGN mid-infrared spectrum. Two other sources have similarly unambiguous powerful PAH, star-dominated mid-infrared spectra. If the infrared counterpart is the power source for the LAB, it is difficult to see how there could possibly be a single explanation for what powers all LABs. Evolutionary scenarios that leave the Lyα halo behind while the internal galaxy changes over to a new energy source (like an AGN turning on) are probably not viable due to the rapid cooling time of the ionized gas halo (∼1–2 Myr). We note that for LAB6_J2143−4423 there is both an AGN and a star-formation-dominated counterpart, so those particular IRS spectra do not contradict the single power source model.

The estimated star formation rates for the PAH-emitting LABs generate enough energy in supernova outflows to power two of the five LABs we observed using IRS. Neither AGN nor cooling flows are needed to explain the Lyα emission for these powerful PAH sources. More generally, cooling flow models may deposit too much mass onto their galaxies, depending on the exact duty cycle of the Lyα halo (Geach et al. 2009). However, there are several well studied, bright LABs with no obvious infrared power source (Smith & Jarvis 2007; Nilsson et al. 2006; Prescott et al. 2009), for which cooling flows remain the most viable explanation.

While more study is certainly required, we would suggest that the data to date do not point to a single, uniform source of power for the LAB. Instead of being a homogenous group of objects, all created in the same way, the LABs are likely a heterogenous group, with different power sources depending on the object. What LABs likely all have in common is their environment: the dense, gas-rich infall zones at the centers of high-redshift overdensities where the most massive galaxies are being born. Outflows or photoionization from intense star formation may drive the majority, but AGNs almost certainly play an important role in others. Cooling flows could account for only a small minority of those seen, which would allow shorter duty cycles and fewer issues of mass deposition.

REFERENCES

Armus, L., et al. 2007, ApJ, 656, 148
Basu-Zych, A., & Scharf, C. 2004, ApJ, 615, L85
Beelen, A., et al. 2008, A&A, 485, 645
Bertone, S., & Schaye, J. 2010, arXiv:1008.1791
Bower, R. G., et al. 2004, MNRAS, 351, 63
Brandl, B. R., et al. 2006, ApJ, 653, 1129
Bruzual, G., & Charlot, S. 2003, MNRAS, 344, 1000
Chapman, S. C., et al. 2004, ApJ, 606, 85
Chary, R., & Elbaz, D. 2001, ApJ, 556, 562
Colbert, J. W., Malkan, M. A., & Rich, R. M. 2006a, ApJ, 648, 250
Colbert, J. W., Teplitz, H., Francis, P., Palunas, P., Williger, G. M., & Woodgate, B. 2006b, ApJ, 637, L89
Dey, A., et al. 2005, ApJ, 629, 654
Dijkstra, M., Haiman, Z., & Spaans, M. 2006, ApJ, 649, 37
Fadda, D., et al. 2010, ApJ, 719, 425
Francis, P. J., et al. 2001, ApJ, 554, 1001
Galliano, F., Madden, S. C., Jones, A. P., Wilson, C. D., Bernard, J.-P., & Le Peintre, F. 2003, A&A, 407, 159
Geach, J. E., Smail, I., Chapman, S. C., Alexander, D. M., Blain, A. W., Stott, J. P., & Ivison, R. J. 2007, ApJ, 655, L9
Geach, J. E., et al. 2005, MNRAS, 363, 1398
Geach, J. E., et al. 2009, ApJ, 700, 1
Güsten, R., Nyman, L. Å., Schilke, P., Menten, K., Cesarsky, C., & Booth, R. 2006, A&A, 454, L13
Haiman, Z., Spaans, M., & Quataert, E. 2000, ApJ, 537, L5
Huang, J.-S., et al. 2009, ApJ, 700, 183
Hunt, L. K., Giovanardi, C., & Helou, G. 2002, A&A, 394, 873
Keel, W. C., White, R. E., Chapman, S., & Windhorst, R. A. 2009, AJ, 138, 986
Keel, W. C., et al. 1999, AJ, 118, 2547
Kohno, K., et al. 2008, in ASP Conf. Ser. 399, Panoramic Views of Galaxy Formation and Evolution, ed. T. Kodama, T. Yamada, & K. Aoki (San Francisco, CA: ASP), 264
Kriek, M., van der Wel, A., van Dokkum, P. G., Franx, M., & Illingworth, G. D. 2008, ApJ, 682, 896
Lacy, M., et al. 2004, ApJS, 154, 166
Lutz, D., et al. 1998, ApJ, 505, L103
Makovoz, D., & Marleau, F. R. 2005, PASP, 117, 1113
Matsuda, Y., Iono, D., Ohta, K., Yamada, T., Kawabe, R., Hayashino, T., Peck, A. B., & Petitpas, G. R. 2007, ApJ, 667, 667

Matsuda, Y., et al. 2004, AJ, 128, 569
Matsuda, Y., et al. 2009, MNRAS, 400, L66
Mori, M., & Umemura, M. 2007, Ap&SS, 311, 111
Murphy, E. J., Chary, R.-R., Alexander, D. M., Dickinson, M., Magnelli, B., Morrison, G., Pope, A., & Teplitz, H. I. 2009, ApJ, 698, 1380
Narayanan, D., Hayward, C. C., Cox, T. J., Hernquist, L., Jonsson, P., Younger, J. D., & Groves, B. 2010, MNRAS, 401, 1613
Nilsson, K. K., Fynbo, J. P. U., Møller, P., Sommer-Larsen, J., & Ledoux, C. 2006, A&A, 452, L23
Ohyama, Y., & Taniguchi, Y. 2004, AJ, 127, 1313
Palunas, P., et al. 2004, ApJ, 602, 545
Papovich, C., et al. 2006, ApJ, 640, 92
Pascarelle, S. M., Windhorst, R. A., Driver, S. P., Ostrander, E. J., & Keel, W. C. 1996, ApJ, 456, L21
Pope, A., et al. 2006, MNRAS, 370, 1185
Pope, A., et al. 2008, ApJ, 675, 1171
Prescott, M. K. M., Dey, A., & Jannuzi, B. T. 2009, ApJ, 702, 554
Prescott, M. K. M., Kashikawa, N., Dey, A., & Matsuda, Y. 2008, ApJ, 678, L77
Rigopoulou, D., Spoon, H. W. W., Genzel, R., Lutz, D., Moorwood, A. F. M., & Tran, Q. D. 1999, AJ, 118, 2625
Saito, T., Shimasaku, K., Okamura, S., Ouchi, M., Akiyama, M., & Yoshida, M. 2006, ApJ, 648, 54
Sajina, A., Yan, L., Armus, L., Choi, P., Fadda, D., Helou, G., & Spoon, H. 2007, ApJ, 664, 713
Scarlata, C., et al. 2009, ApJ, 706, 1241
Siringo, G., et al. 2007, The Messenger, 129, 2
Siringo, G., et al. 2008, Proc. SPIE, 7020, 702003
Smail, I., Ivison, R. J., Gilbank, D. G., Dunlop, J. S., Keel, W. C., Motohara, K., & Stevens, J. A. 2003, ApJ, 583, 551
Smith, D. J. B., & Jarvis, M. J. 2007, MNRAS, 378, L49
Smith, D. J. B., Jarvis, M. J., Lacy, M., & Martínez-Sansigre, A. 2008, MNRAS, 389, 799
Smith, J. D. T., et al. 2007, ApJ, 656, 770
Steidel, C. C., et al. 2000, ApJ, 532, 170
Stern, D., et al. 2005, ApJ, 631, 163
Stern, D., et al. 2007, ApJ, 663, 677
Stewart, K. R., Bullock, J. S., Wechsler, R. H., & Maller, A. H. 2009, ApJ, 702, 307
Taniguchi, Y., & Shioya, Y. 2000, ApJ, 532, L13
Thornton, K., Gaudlitz, M., Janka, H.-T., & Steinmetz, M. 1998, ApJ, 500, 95
Uchimoto, Y. K., et al. 2008, PASJ, 60, 683
Webb, T. M. A., Yamada, T., Huang, J.-S., Ashby, M. L. N., Matsuda, Y., Egami, E., Gonzalez, M., & Hayashimo, T. 2009, ApJ, 692, 1561
Weijmans, A.-M., Bower, R. G., Geach, J. E., Swinbank, A. M., Wilman, R. J., de Zeeuw, P. T., & Morris, S. L. 2010, MNRAS, 402, 2245
Wilman, R. J., Gerssen, J., Bower, R. G., Morris, S. L., Bacon, R., de Zeeuw, P. T., & Davies, R. L. 2005, Nature, 436, 227
Yang, Y., Zabludoff, A., Tremonti, C., Eisenstein, D., & Davé, R. 2009, ApJ, 693, 1579
Yan, L., et al. 2007, ApJ, 658, 778
Yun, M. S., et al. 2008, MNRAS, 389, 333